The effects of buoyancy on shear-induced melt bands in a compacting porous medium

S.L. Butler [a,*]

[a] *Department of Geological Sciences, University of Saskatchewan, 114 Science Place, Saskatoon, SK, S7N 5E2, Canada*

Abstract

It has recently been shown (*Holtzmann et al.* (2003) and *Holtzmann and Kohlstedt* (2007)) that when partially molten rock is subjected to simple shear, bands of high and low porosity are formed at a particular angle to the direction of instantaneous maximum extension. These have been modeled numerically and it has been speculated that high porosity bands may form an interconnected network with a bulk, effective permeability that is enhanced in a direction parallel to the bands. As a result, the bands may act to focus mantle melt towards the axis of mid-ocean ridges (*Katz et al.* (2006)). In this contribution, we examine the combined effects of buoyancy and matrix shear on a deforming porous layer. The linear theory of *Spiegelman*, (1993), *Spiegelman* (2003) and *Katz et al.* (2006) is generalized to include both the effects of buoyancy and matrix shear on a deformable porous layer with strain-rate dependent rheology. The predictions of linear theory are compared with the early time evolution of our 2D numerical model and they are found to be in excellent agreement. For conditions similar to the upper mantle, buoyancy forces can be similar to or much greater than matrix shear-induced forces. The results of the numerical model indicate that bands form when buoyancy forces are large and that these can significantly alter the direction of the flow of liquid away from vertical. The bands form at angles similar to the angle of maximum instantaneous growth rate. Consequently, for strongly strain-rate dependent rheology, there may be two sets of bands formed that are symmetric about the direction of maximum compressive stress in the background mantle flow. This second set of bands would reduce the efficiency with which melt bands would focus melts towards the ridge axis.

* Corresponding author. Fax:+1-306-966-8593
Email address: sam.butler@usask.ca (S.L. Butler).

1 Introduction

Holtzmann et al. (2003) and *Holtzmann and Kohlstedt* (2007) presented experiments in which partially molten ductile rocks were subjected to deformation approximating simple shear. It was found that if the size of the sample was similar to or greater than the compaction length, high porosity bands would spontaneously form at angles of roughly 20^o to the shear plane. If a sample of a partially molten material is larger than its compaction length, a significant degree of matrix deformation will take place if the sample is subjected to an applied stress (*Mckenzie*, 1984). Stevenson (1989) had shown theoretically that partially molten materials should spontaneously segregate into high and low porosity regions provided that the viscosity of the solid matrix is a decreasing function of porosity when the matrix is subjected to pure shear. The formation of bands, perpendicular to the direction of maximum extension, in simulations of shear flow in strain independent but porosity weakening rheology, was demonstrated by *Richardson* (1998). *Richardson* (1998) also included the effects of buoyancy and showed that veins formed when buoyancy was active and that background shear resulted in the elongation in the direction of maximum compressive stress of a rising porosity solitary wave. *Spiegelmen* (2003) and *Katz et al.* (2006) showed using linear theory and numerical simulations that such bands will grow and that the angle at which the bands grow fastest is a function of the strain-rate dependence of the viscosity of the matrix. They found that if the exponent relating the viscosity to the strain rate is roughly four or greater, that the melt bands form at low angles similar to the ones seen in the experiments.

Melting is believed to occur in roughly the top 60 km in the upwelling region below the ridge axis (*Hess*, 1992). The lateral extent of melting is believed to be roughly 100 km (*Forsyth et al.*, 1998) while melts are mostly extracted within 1 km of the ridge axis (*Vera et al.*, 1990). A number of mechanisms have been proposed to explain the focusing of mantle melt towards the ridge axis. These include the stresses imparted on the interstitial fluid by the background circulation of the solid mantle matrix (*Phipps-Morgan*, 1987; *Spiegelman and Mckenzie*, 1987), a decompaction channel beneath the near surface mantle solidus (*Sparks and Parementier*, 1991) and anisotropic permeability induced by the strain due to the mantle circulation (*Phipps-Morgan*, 1987). *Katz et al.* (2006) noted that if melt bands form in the mantle below mid-ocean ridges and they are rotated by 25^o from the direction of maximum compressive stress, as they are in the experiments and in the numerical simulations with highly strain-rate dependent viscosity, that they could act as a network of interconnecting high permeability pathways channeling melt towards the ridge axis.

One effect of buoyancy on a compacting porous medium is to induce oscillations and waves (e.g., *Scott and Stevenson*, 1986; *Spiegelman*, 1993). Where

buoyancy-driven flow encounters a region of reduced permeability, fluid will build up leading to an increase in the porosity and permeability. As a result, more fluid will be drawn into this region, decreasing the porosity and permeability in the surrounding regions and resulting in propagating regions of increased and reduced porosity and permeability. It is the main purpose of this paper to investigate the interaction of this effect with strain-induced porosity localization. In agreement with *Richardson* (1998) we will show that bands can form in the presence of buoyancy and we will demonstrate that their growth rate is not affected by the degree of buoyancy. We will also show that strain-induced melt bands can channel flow in directions away from vertical. However, for highly strain-rate dependent viscosity there may be two different orientations of melt bands.

In what follows, the governing equations for the numerical simulations will first be presented. We will then present the linear theory of a compacting porous layer under the influence of an externally imposed simple shear and buoyancy when the matrix viscosity can be strain-rate dependent in section 3 and we will compare some predictions of linear theory with the numerical model results. In section 4, the results of numerical simulations with various degrees of strain-rate dependence of viscosity and buoyancy driven flow will be presented. Section 5 contains some interpretation and discussion of our results.

2 Governing Equations

We solve the dimensionless equations appropriate for a compacting porous layer (e.g., *McKenzie*, 1984; *Scott and Stevenson*, 1984) in two space dimensions, x and y in a square domain of side length two compaction lengths centered on the origin. We impose a background, simple-shear, velocity of the solid matrix and fluid of the form $U_0 = ysin(\theta)$, $V_0 = xcos(\theta)$. Here θ can either be 0 or $\pi/2$ corresponding to shear in the vertical and horizontal directions. Our methodology can be easily generalized to other background flow geometries.

The dimensionless equations for the force balance of the fluid phase and for the solid matrix are

$$\phi(\mathbf{u} - \mathbf{U}) = -k_\phi(\nabla p - (1 - \phi_0)B_u\hat{j}) \tag{1}$$

and

$$\nabla \cdot \begin{pmatrix} -p + \frac{\zeta+\frac{4}{3}\eta}{\zeta+\frac{4}{3}}\frac{\partial U}{\partial x} + \frac{\zeta-\frac{2}{3}\eta}{\zeta+\frac{4}{3}}\frac{\partial V}{\partial y} & \frac{\eta}{\zeta+\frac{4}{3}}(\frac{\partial U}{\partial y} + \frac{\partial V}{\partial x} + 1) \\ \frac{\eta}{\zeta+\frac{4}{3}}(\frac{\partial U}{\partial y} + \frac{\partial V}{\partial x} + 1) & -p + \frac{\zeta+\frac{4}{3}\eta}{\zeta+\frac{4}{3}}\frac{\partial V}{\partial y} + \frac{\zeta-\frac{2}{3}\eta}{\zeta+\frac{4}{3}}\frac{\partial U}{\partial x} \end{pmatrix} = \begin{pmatrix} 0 \\ (\phi_0 - \phi)B_u \end{pmatrix}. \quad (2)$$

While equations indicating that the combined fluid and solid are incompressible and a mass conservation equation for the solid can be written

$$\nabla \cdot [\mathbf{u}\phi + \mathbf{U}(1-\phi)] = 0 \quad (3)$$

and

$$\frac{\partial \phi}{\partial t} = \nabla \cdot [(\mathbf{U} + y\sin(\theta)\hat{i} + x\cos(\theta)\hat{j})(1-\phi)]. \quad (4)$$

Here $\mathbf{u}$ and $\mathbf{U} = [U, V]$ represent velocity variations from the background flow for the fluid and solid phases, and p and ϕ are the transformed fluid pressure (see below) and the porosity while $\hat{i}$ and $\hat{j}$ are unit vectors in the horizontal and vertical directions. The equations are made dimensionless using scales for length, pressure, velocity and viscosity of δ_c, $\dot{\gamma}(\zeta_0 + 4/3\eta_0)$, $\dot{\gamma}\delta_c$ and η_0 where δ_c is the compaction length, $\dot{\gamma}$ is the strain rate corresponding to the background velocity and ζ_0 and η_0 are the dimensional bulk and shear viscosity of the matrix at the initial porosity and background strain. The parameters ζ and η represent the dimensionless bulk and shear viscosities. The compaction length is given by $\delta_c = (k_0(\zeta_0 + 4/3\eta_0)/\mu)^{0.5}$ where k_0 is the permeability at the initial porosity, and μ is the liquid viscosity. Both ζ and μ are assumed to be constant. *Katz et al* (2006) reported simulations with and without a porosity dependence of the bulk viscosity and found very little resulting differences.

The transformed pressure, p, is related to the fluid pressure, p_{fluid}, by $p = p_{fluid} + [(1-\phi_0)\rho_s + \phi_0\rho_l]B_u y$ where ρ_s and ρ_l are the dimensional solid and fluid densities divided by the difference between the solid and fluid densities and ϕ_0 is the initial background porosity. The dimensionless parameter B_u is defined in the following section. The pressure is transformed in this way so that the mean difference in p between the top and bottom boundaries is 0. This allows us to use periodic vertical boundary conditions.

The shear viscosity of the matrix is taken to weaken with porosity (*Mei et al.*, 2002) and strain-rate (*Karato and Wu*, 1993) according to

$$\eta = \exp(\alpha(\phi - \phi_0))[\sqrt{2}(\frac{\partial U}{\partial x}^2 + \frac{\partial V}{\partial y}^2 + 0.5(\frac{\partial U}{\partial y} + \frac{\partial V}{\partial x} + 1)^2)^{0.5}]^{\frac{1-n_v}{n_v}}. \quad (5)$$

The parameter α is taken to be -25 (*Mei et al.*, 2002) while the factor of $\sqrt{2}$ causes the dimensionless viscosity to be 1 when the velocity of the solid is equal to the background value. The value of the strain-rate exponent, n_v, is varied from one simulation to another from a minimum value of 1 (strain-rate-independent viscosity) to a maximum value of 6. Recently, *Korenaga and Karato* (2008) have reported preferred values of n_v of 3.6 and 4.94 for wet and dry dislocation creep of mantle olivine that are somewhat higher than the values of 3.5 and 3.5 preferred by *Hirth and Kohlstedt* (2003).

The dimensionless permeability is taken to be of the form $k_\phi = (\phi/\phi_0)^n$, which is a simplified form of the Cozeny-Carmen relationship (*Carmen*, 1939), where n is taken to be 3 for all of the simulations presented here.

All of the dependent variables ($\mathbf{u}$, $\mathbf{U}$, p and ϕ) are required to be periodic in both the horizontal and vertical directions. Periodic vertical boundary conditions are useful when investigating the effects of gravity since otherwise some solid material would be entering and leaving the solution domain. In all of the results presented the shear plane is in the horizontal direction ($\theta = 90^o$) (i.e., the shear plane is perpendicular to gravity) except for one set where we investigate the effects of having the shear plane parallel to gravity and $\theta = 0$. The governing equations were solved using the commercial finite element modeling package COMSOL using 3184 triangular elements. A few simulations were repeated with doubled resolution. The growth rates for the bands for the high and low resolution simulations were indistinguishable and the angles at which the bands were formed were also very similar. However, as will be shown, the growth rate of the bands increases with their wavenumber but becomes constant provided that the wavelength is much smaller than the compaction length. Since higher resolution simulations capture shorter wavelength variations, the wavelength of the bands was observed to be reduced in higher resolution simulations if the imposed initial porosity perturbation contained wavelengths that were smaller than could be resolved in the lower resolution simulations.

2.1 Dimensionless Parameters

The dimensionless parameters for this system include L/δ_c, the size of the solution domain measured in compaction lengths, ζ, the ratio of the bulk viscosity to the initial shear viscosity, ϕ_0, the initial porosity, and a buoyancy parameter, $B_u = (g\Delta\rho\delta_c)[(\zeta_0 + 4/3\eta_0)\dot{\gamma}]^{-1}$, where g is the acceleration due to gravity and $\Delta\rho$ is the difference in density between the liquid and solid.

In the experiments of *Holtzman et al.* (2003), it was shown that porosity bands formed in sheared samples provided that L/δ_c was of order 1 or greater. Phys-

ically, if the system is much smaller than the compaction length, an applied stress will cause motion of the fluid relative to the matrix but little deformation of the matrix. In all of the simulations presented here, both horizontal and vertical dimensions of the simulation area are taken to have dimensionless values of two. The compaction length in the upper mantle below mid-ocean ridges is estimated to be in the range, 100 m $< \delta_c <$ 10 km (e.g., *Holtzmann et al.*, 2003), as such, our simulation domain represents a small "window" of this region of the Earth.

The bulk viscosity of mantle materials is still poorly constrained but likely lies in the range 1-10 times the shear viscosity (*Cooper*, 1990; *Renner et al.*, 2003). As will be seen in the following section, increasing ζ has the effect of decreasing the growth rate of melt bands. All of the simulations reported herein use a value of $\zeta = 1$.

The initial porosity of all of the simulations was taken to be 0.01, a value appropriate for the region of decompression melting in the upper mantle (*Hammond and Tomey*, 2003).

The parameter B_u is the ratio of buoyancy forces to stresses caused by the induced strain. In figure 1, contours of B_u are plotted as a function of position in the vicinity of a fast-spreading mid-ocean ridge (black contours). The compaction length is assumed to be 1 km, the viscosity is assumed to be 10^{19} Pas (*Korenaga and Karato*, 2008), the the plate is assumed to move at 7.5 cm/yr while $g = 10$ m/s^2 and $\Delta\rho = 500$ kg /m^3 (*Guillot and Sator*, 2007). We employ the constant viscosity, corner flow model of *Spiegelman and McKenzie* (1987) and contours of the stream function have also been included (blue lines) as well as the integrated total shear strain (red lines). It can be seen that B_u is largest near the center of upwelling where there is very little shear and decreases moving laterally away from the upwelling and radially away from the ridge crest. The effects of buoyancy are seen to be significant everywhere within the mantle melt zone, however, and are even larger near slow-spreading ridges. There is significant uncertainty in the value of many of the parameters used to calculated B_u, particularly 100 m $< \delta_c <$ 10 km and 10^{19} Pa s $< \eta_0 < 10^{21}$ and as stated previously, the value of ζ_0 is very poorly constrained. Within the range of uncertainly for parameters that make up B_u, buoyancy forces are only important in the low-strain vicinity of the sub-ridge mantle upwelling or they may be dominant everywhere. In the experiments of *Holtzmann et al.* (2003), $B_u \simeq 10^{-8}$, and the effects of buoyancy were negligible since the strain rates were high compared with mantle values. The total shear strain was calculated by integrating the shear strain rate with time along fluid particle trajectories starting at 60 km depth.

3 Linear Theory

The linear theory of a deformable porous layer subject to the effects of gravity-induced buoyancy in the absence of matrix shear and strain-rate dependent viscosty has been investigated by *Scott and Stevenson* (1986) and *Spiegelman* (1993). The effects of simple shear of the solid matrix were investigated by *Spiegelman* (2003) while *Katz et al.* (2006) included the effects of non-Newtonian viscosity. The development of a linear theory is useful in that it aids significantly in the development of our physical understanding of the system and it provides tests of the early time evolution of the full non-linear numerical model.

Following the linear theory presented in the above mentioned papers, it can be shown that to first order, the porosity of a plane wave will evolve with time according to

$$\phi = \phi_0 + \Delta\phi \exp[i(k_x x + k_y y - \Omega(t)) + s(t)] \tag{6}$$

where $k_x = k_x^0$, $k_y = k_y^0 - k_x^0 t$, are the time-dependent wavenumbers in the x and y directions and k_x^0 and k_y^0 are their values at time 0 while $\Delta\phi$ is the magnitude of the porosity perturbation. As was shown by *Spiegelman* (2003) these wavenumbers represent a plane wave that rotates with the shear flow in time. The instantaneous frequency, ω, is given by

$$\omega = \frac{\partial\Omega}{\partial t} =$$

$$B_u(1-\phi_0)\frac{[k^4 + \frac{1-n_v}{n_v}(k_x^2 - k_y^2)^2][\frac{[n(1-\phi_0)-\phi_0]k_y}{\phi_0}] + 2\frac{1-n_v}{n_v}k_x^2 k_y(k_x^2 - k_y^2)}{(k^2+1)[k^4 + \frac{1-n_v}{n_v}(k_x^2 - k_y^2)^2] + 4\frac{1-n_v}{n_v}\xi k_x^2 k_y^2 k^2}, \tag{7}$$

which for the case of linear rheology reduces to

$$\omega = B_u(1-\phi_0)\frac{[n(1-\phi_0)-\phi_0]k_y}{(k^2+1)\phi_0}, \tag{8}$$

which is the same as the form obtained by *Spiegelman* (1993). The instantaneous growth rate is given by

$$\frac{ds}{dt} = -2\xi\alpha(1-\phi_0)\frac{k_x k_y k^4}{(k^2+1)[k^4 + \frac{1-n_v}{n_v}(k_x^2 - k_y^2)^2] + 4\frac{1-n_v}{n_v}\xi k_x^2 k_y^2 k^2} \tag{9}$$

(*Katz et al.*, 2006) where $\xi = \frac{1}{\zeta+4/3}$. The amplitude of the plane wave as a function of time is given by $\exp[s]$. When the rheology of the matrix is linear

($n_v = 1$) there is an analytical expression for this amplitude, however, when $n_v \neq 1$, equation 9 must be integrated numerically. The characteristic growth time can be estimated from the growth rate at time 0 by $1/\frac{ds}{dt}(0)$ while the period of oscillation is given by $2\pi/\omega(0)$. For a range of other parameter values, the growth time and oscillation period are similar when B_u is of order 1.

In figure 2 we show a contour plot of ω with an overlain arrow plot of $\nabla_k \omega = \mathbf{v_g}$ where $\mathbf{v_g}$ is the group velocity of a wave packet, calculated with $n_v = 6$. In our numerical simulations, the minimum wavenumber (based on a system size of 2) is π so wavelengths smaller than this have been excluded in figure 2. Also, only bands with $k_x * k_y > 0$ grow when subjected to shear as can be seen from equation 9 and the fact that $\alpha < 0$. As a result, only the first quadrant has been shown. As can be seen, waves in this wavenumber range all propagate to the left. The propagation direction has an upward component if k_y is small compared with k_x and downward otherwise. It can also be seen that shorter wavelengths propagate much faster than long ones. The group velocity pattern over this range was similar for different values of n_v. The possibility of downward propagating porosity waves was also discussed by *Spiegelman* (1993) and the results presented are similar to those presented in that paper except that the range over which we have plotted our wavenumbers is significantly higher.

As can be seen in equation 9, the growth rate in linear theory is not affected by buoyancy. Equation 9 indicates that if $|k| \gg 1$, which is roughly equivalent to the wavelength being much less than the compaction length, the growth rate is independent of the magnitude of the wavenumber. *Hall and Parmentier* (2000) argued that the grain size controls the wavelength of the initial melt heterogeneity which would mean that these very small wavelength fluctuations would be amplified and would not produce longer wavelength heterogeneity unless another mechanism were present. These authors argued further that the effects of increasing matrix viscosity with melting-induced matrix dehydration could increase the length scale of these porosity instabilities. The laboratory experiments of *Holtzmann et al.* (2003) indicated that the compaction length of the sample controls the spacing of the shear bands which indicates that either the compaction length sets the length scale of the initial heterogeneity or some physics such as surface tension, that is not present in the current model is important in the experiments. *Spiegelman* (2003) demonstrated that the angle of maximum growth rate is 45^o to the shear plane, or parallel to the direction of maximum compression, for linear rheology for a sample subjected to simple shear. When viscosity is strain-rate dependent, there can be two angles of instantaneous maximum growth rate, which for $n_v = 3.5$ and 6 are oriented $\pm 17^o$ and $\pm 27^o$ to the direction of maximum compression when $\zeta = 1$ and $|k| \gg 1$. In a simple shear flow, lines that are close to parallel to the shear plane rotate more slowly than those that are steeper. Because of this, and because they are already closer to 90^o, high angle bands will quickly rotate

beyond 90^o at which point they will decay in amplitude (*Spiegelman*, 2003). As we will show in the following section, in the presence of a significant degree of buoyancy, the high angle bands remain significant at finite strain.

A few simulations were initiated with plane wave initial conditions (e.g. $\phi = \phi_0 + \Delta\phi \cos[k_x^0 x + k_y^0 y]$) in order to test the numerical model. In figure 3, we display the natural logarithm of the amplitude of the porosity varition as a function of time, or total strain, calculated from the numerical model from

$$Amp = [\frac{\int(\phi(t) - \phi_0)^2 dA}{\int(\phi(t=0) - \phi_0)^2 dA}]^{0.5} \tag{10}$$

and compare it with a numerical integration of equation 9. Here we take $\alpha = -25$, $\zeta = 1$ and $k_x^0 = k_y^0 = 4\pi$ for $n_v = 1$, 3.5 and 6 and $B_u = 0$. It can be seen that for linear rheology, the agreement is excellent up to a strain of 0.8 whereupon the linear solution approaches a maximum at a strain of one and then start to decrease while the numerical solution continues to increase. The growth rate of the linear solution decreases and then becomes negative as the bands rotate with the shear flow since the growth rate is a strong function of the orientation of the porosity bands. In the numerical simulation, the bands break and then reform at angles favorable for growth so that growth continues. For strain-rate dependent rheologies, the amplitude of the porosity bands remains in good agreement with the linear theory throughout the time of the simulations. It can be seen that the porosity bands grow more rapidly as the strain-rate dependence of the matrix viscosity increases. Simulations with different values of n_v, ζ, ϕ_0 and initial wavenumber were also initiated with similar agreement between the linear theory and the simulation.

In figure 4 the results of a simulation with $Bu = 10$ and $n_v = 6$ that was initiated with a plane wave solution with $k_x = k_y = 4\pi$ are shown. The dashed lines show the amplitude envelope predicted from equation 9 while the dotted line represents the product of this envelope with an oscillatory term of the form $\cos(\Omega(t))$. The solid line represents the porosity increase at the center of the domain calculated from the numerical model. It can be seen that up to a time of 0.15, the porosity of the numerical simulation evolves essentially as is predicted by linear theory whereupon the amplitude of the linear theory fluctuations starts to excede those of the numerical model. The traveling porosity waves are causing the oscillations in the porosity at a point while the shear is causing the increase in amplitude. As can be seen from equation 7, the oscillation frequency is 0 for vertically oriented bands ($k_y = 0$). For $n_v = 1$ and 6, bands oriented at 0 and 23^o to horizontal oscillated at the highest frequency. As a result, the oscillation frequency for these bands, which started at 45^o to the shear plane, decreases and in linear theory it will pass through 0 and experience a phase shift of 180^o. In the numerical model, the bands will break and reform at lower angles so the oscillations never go through

a phase shift.

4 Numerical Results

A series of simulations were initiated with white noise random initial variations from the background porosity of amplitude $\Delta\phi = \phi_0 \times 10^{-6}$ with various values of B_u and $n_v = 1$, 3.5 and 6. In figure 5, the porosity field at a strain of 0.88 is shown for a simulation with a low buoyancy number of $B_u = 0.1$ and $n_v = 6$. As can be seen, the porosity field is distributed in bands of enhanced and depleted porosity that are at an angle of roughly 20^o, similar to what is reported in the experiments of *Holtzmann et al.* (2003) and *Holtzmann et al.* (2007) and the numerical simulations of *Katz et al.* (2006). The magenta arrows indicate the velocity of the liquid and it can be seen that the motion of the liquid has been deflected from vertical and the fluid velocity is highest along high porosity and hence high permeability pathways. This indicates that for low values of B_u or high ratios of the background strain forces to buoyancy forces, bands continue to form and they are capable of focussing the flow of the liquid phase. This and all other finite amplitude simulations terminated when the porosity became 0 in some region, at which time the maximum porosity was roughly $2\phi_0$.

In figure 6 we plot the natural logarithm of the amplitude of the porosity localization as defined in equation 10 for simulations with $n_v = 6$ and $n_v = 1$ for the values of B_u indicated. We also plot the amplitude as predicted from the growth rate calculated from equation 9 at angles of 45 and 18^o to the shear plane which represent the angles of maximum growth rate when $n_v = 1$ and 6 when $|k|$ is large (dotted symbols). As can be seen, the porosity variations in calculations with $B_u = 0$ (dash-dot line) grow somewhat faster initially but all of the simulations with the same n_v follow essentially the same exponential porosity heterogeneity growth thereafter. The presence of buoyancy and porosity waves does not inhibit the porosity localization and, as predicted by equation 9, the growth rate is increased when using larger n_v. A series of models with $n_v = 3.5$ were also run that showed a similar pattern of porosity variation growth with a growth rate that was intermediate between those with $n_v = 1$ and $n_v = 6$. It can also be seen that when $n_v = 1$, the bands grow somewhat more slowly than the fastest growing mode of linear theory indicating that the bands get rotated by the background flow away from the orientation of fastest growth rate. The run with $B_u = 10$ has the steepest slope, however, which occurs because, as we will show, bands stay close to the orientation of maximum growth rate when buoyancy-induced oscillations are present.

In figures 7a and 7b the porosity field (colors) and liquid velocity fields (arrows)

are plotted for simulations with $B_u = 10$ and $n_v = 3.5$ and 6, respectively. At this high value of B_u, the porosity patterns oscillate rapidly and traveling waves occur that propagate mostly downward and to the left, as predicted by the linear theory. The pattern of bands for the $n_v = 3.5$ case is very similar to what is seen at smaller values of B_u and the mean orientation of the bands is roughly 45^o. As can be seen, these bands are made up of interconnected segments that are oriented at roughly 30^o and 60^o to the shear plane. For the calculation with $n_v = 6$ it can be seen that there is now an interconnected network of bands at roughly 20 and 70^o to the shear plane. The bands at 70^o are absent in the calculation at low B_u (see figure 5).

The power spectrum as a function of angle to the shear plane is plotted as a function of time in figures 8a and b for calculations with $B_u = 0.1$ and $B_u = 10$. The power spectrum was calculated by integrating the amplitude of the fourier transform at each value of the angle to the shear plane. We plot the angle from the shear plane along the horizontal axis and time along the vertical axis and we have normalized the power spectrum at each value of time. The angle is only plotted up to 90^o since there is very little power for angles between 90^o and 180^o. As can be seen, the amplitude spectrum is sharply peaked at 20^o for the low buoyancy case with $n_v = 6$ but when the buoyancy number is 10, the high angle bands at roughly 70^o contain as much power as the low angle ones leading to a bimodal amplitude distribution as a function of angle.

In figure 9 we display the amplitude spectrum averaged over the latter half of simulations. Figure 9c displays the results of a calculation with $n_v = 6$ for $B_u = 0$ (dashed-dot line), 0.1 (dotted line), 1 (solid line) and 10 (dashed line) as well as the prediction of linear theory for the instantaneous growth rate as a function of band angle (solid line with circles). It can be seen that as B_u is increased, the low angle peak decreases in magnitude while the second peak at roughly 70^o becomes increasingly prominent. In the absence of buoyancy effects, the high angle band will quickly rotate beyond 90^o after which it will decay and disappear. In the presence of significant buoyancy, the bands are no longer strongly rotated by the background flow and the high angle band becomes significant once more. The condition for the bands to not be rotated by the background shear is that the period of the buoyancy oscillations is significantly less than the time taken for matrix shear. A possible explanation for the decoupling of the bands from the background shear is that many new nucleation sites for strain-induced porosity localization arise due to the oscillations and these cause new bands to form in orientations for which the bands will grow at the fastest rates. In figures 9a and 9b we show similar plots for $n_v = 1$ and $n_v = 3.5$. When the viscosity is only porosity dependent, it can be seen that for low values of B_u, the peak power is higher than 45^o. This arises because the bands initially form at 45^o but get rotated by the shear flow to a steeper angle before they break and reform again at 45^o. The low B_u bands

for $n_v = 6$ at 20^0 are not rotated as strongly because these are less affected by rotation in simple shear flows. When $B_u = 10$ and $n_v = 1$, the peak power remains at 45^o, which occurs because the bands become decoupled from the background rotation in the presence of strong porosity oscillations and so the bands remain in the orientation of maximum growth rate. As can be seen in figure 9b, there is a very broad distribution of power for all values of B_u when $n_v = 3.5$ and the distribution is not significantly changed by the presence of buoyancy. Linear theory predicts two very weak peaks in growth rate for bands at angles of 28 and 62^o which are clearly too close together and too broad to be resolved by the fourier analysis.

The results of model runs for which the shear plane is parallel to gravity ($\theta = 0$) are presented in figures 10 a) and b) for calculations with $n_v = 6$ and $B_u = 0.1$ and $B_u = 10$ at a total strain of 0.92. As can be seen in the figures, only bands at roughly 20^o to the shear plane, which is parallel to gravity, occur when $B_u = 0.1$ and the buoyancy-driven fluid flow is concentrated within the high porosity bands resulting in a slight deflection of the flow from vertical. When $B_u = 10$ there is a second set of bands oriented at roughly 70^o to the shear plane. This indicates that bands will form roughly at the angle of maximum instantaneous growth rate, regardless of their orientation relative to gravity, provided that the degree of buoyancy forcing is sufficiently high.

In order to test the generality of the result that bands will form at particular angles to the direction of maximum extension, a further set of simulations was undertaken using a pure shear background flow ($U_0 = x$, $V_0 = -y$) rather than simple shear. In these simulations, the direction of maximum compression is vertical. In figures 11a) and b) the results of simulations with $B_u = 10$ and $n_v = 1$ and $n_v = 6$ are presented. In figure 11a) it can be seen that vertical linear bands form, parallel to the direction of maximum compression, and that the fluid flow is enhanced in the high porosity bands. When $k_y = 0$ equation 7 indicates that the oscillation frequency should be zero and, in agreement with the linear theory, these bands were not observed to oscillate significantly despite the high degree of buoyancy forcing. A similar run (not shown) was undertaken with the direction of maximum compression in the horizontal direction and horizontal bands were observed. In this latter case, k_x was close to zero and a significant degree of wave motion was observed and the bands were seen to propagate downward in accord with the predictions of linear theory when $k_y > k_x$. In figure 11b) it can be seen that there are two sets of bands that are oriented at roughly $\pm 27^o$ to the direction of maximum compression when $n_v = 6$. As a result, although the background flow over some volume of mantle that is driven by the large scale circulation of the mantle will be significantly more complicated than either pure or simple shear, it would appear that the orientation of the growth of melt bands relative to the direction of maximum compressive shear stress will depend on n_v and B_u only.

5 Discussion and Conclusions

We have shown that in the presence of buoyancy, strain-induced porosity bands continue to form and grow at a rate that is essentially independent of buoyancy forcing. The fluctuations in porosity induced by the waves decouple the waves from the background rotation and the bands maintain an orientation that is very close to the angle of instantaneous maximum growth rate.

Katz et al. (2006) demonstrated that if shear bands form at roughly 20^o to the shear plane and so 25^o to the direction of maximum compression as they do in experiments and in simulations with $n_v = 6$, that the bands form in an appropriate orientation to channel mantle melts towards ridge axes. We have shown that these bands continue to form in the presence of buoyancy-induced oscillation and that these can cause channeling and deflection of the melt flow. We have also shown that if the effects of buoyancy are large and the strain-rate dependence of viscosity is greater than 3.5, there should be two sets of high porosity bands, one oriented so as to focus melt towards the ridge axis and the other oriented roughly 50^o to the first with an orientation that is closer to vertical. These two sets of high porosity and permeability bands would form an interconnected network that would transport melt rapidly to the surface but would be less effective in focussing melt towards the ridge axis than would a set of bands with only a single orientation relative to the direction of maximum compressive stress. Dunites observed in ophiolite complexes have been interpreted to have been high permeability conduits for mantle melts beneath mid ocean ridges (e.g., *Braun and Kelemen*, 2002). These authors interpreted these conduits to arise due to preferential dissolution of pyroxenes in regions of rapidly rising melt and the resultant increase in matrix permeability: the so-called reactive infiltration instability (e.g., *Aharanov et al.*, 1997). If shear induced porosity localization is an important process beneath mid-ocean ridges, then it is likely that the shear bands would act as sites where dissolution would occur first and hence these may act as seed sites for the dunites. If buoyancy-induced waves are important in the formation of the bands then it is predicted that these channels should exist with two particular orientations, provided that the strain-rate dependence of viscosity is greater than roughly four.

As mentioned previously, there is a great deal of uncertainty in the values of the the matrix viscosity and in the appropriate compaction length for the sub-ridge axis mantle. If η_0 is substantially greater or if δ_c is substantially less than the values used in order to calculate the results displayed in figure 1, it is possible that buoyancy will have relatively little effect on the orientation of melt bands. As a further caveat, all of the simulations presented here terminate when the porosity at some point in the simulation domain became 0 at which point the flow field of the liquid had only recently become strongly affected

by the heterogeneous permeability field of the matrix. It is possible that with further time evolution the geometry of the band structure will change once again. The total shear strain experienced by mantle material during its ascent through the melt region in the mantle beneath mid ocean ridges is displayed in figure 1 and is at most 4 and is significantly less for most material trajectories. This indicates that it is unlikely that the melt bands will have time to evolve significantly further. However, the total strain required for melt bands to grow to the extent that they significantly influence the direction of flow of melt is also a function of the amplitude of the initial porosity perturbation, which is difficult to estimate. Also, the wavelength of the bands calculated increases with the wavelength of the initial perturbation. Equation 7 indicates that the oscillation frequency decreases with wavenumber so that lower wavelength bands should oscillate more slowly and hence higher values of B_u will be required to cause significant higher angle bands. *Holtzmann et al.* (2003) found in their experiments that there are roughly five bands per compaction length, which is similar to what we see in our simulations. If the heterogeneity length scale in the mantle does not scale simply from the experiments, the spacing of the bands could be significantly different and so will be the extent to which they are affected by buoyancy-driven flow. Furthermore, the strain rate scales roughly like the mantle matrix velocity so at slow spreading ridges, the total strain may be at most 0.5 which is likely not large enough to result in the formation of significant melt bands.

Another setting of geological importance where compaction phenomena occur is in igneous cumulates in magma chambers (e.g., *Shirley*, 1986). A significant difference between this setting and the mantle beneath mid-ocean ridges is that the porosity may be as large as 0.5 (e.g., *Campbell*, 1978). Examination of equations 7 and 9 indicates that the growth rate decreases slightly when porosity is larger while the frequency of oscillation will be very significantly decreased due to the $1/\phi_0$ term in the numerator of equation 7. Using values of $\Delta\rho = 200$ kg/m^3, $\delta_c = 100$ m, and $\eta = 10^{17}$ Pas (*Shirley*, 1986) we estimate that the strain rate would have to be less than 2×10^{-12}s^{-1} in order for B_u to be of order 1 and for buoyancy forces to be similar to shear forces. This implies extremely small velocity differences over a cumulate pile of any reasonable size and hence it is almost certain that buoyancy-induced waves and oscillations will not be important in magma chambers. A few simulations with porosity of 0.5 were undertaken (not shown) and porosity banding was seen to occur with angles similar to those seen in the lower porosity simulations.

In the future, it will be interesting to incorporate more realistic matrix flow geometries calculated from simulations of large scale mantle convection in the vicinity of mid-ocean ridges and to incorporate the effects of ongoing mantle melting. It would also be useful to examine the combined effects of shear-induced melt localization and melt-rock reactions as these can lead to further flow channeling through the reactive infiltration instability (*Aharanov et al.*,

1997).

References

[1] Aharanov, E., M. Spiegelman and P. Kelemen, Three-dimensional flow and reaction in porous media. Implications for Earth's mantle and sedimentary basins, *J. Geophys. Res.102*, 14821-14833, 1997.

[2] Braun, M.G., P.B. Kelemen, Dunite distribution in the Oman Ophiolite: Implications for melt flux through porous dunite conduits, *Geochem. Geophys. Geosys.*, *3*, doi:10.1029/2001GC000289, 2002.

[3] Campbell, I.H., Some problems with cumulus theory, *Lithos*, *11*, 311-323, 1978.

[4] Carmen, P.C., Permeability of saturated sands soils and clays, *Journal of Agricultural Sciences*, *29*, 262-273, 1939.

[5] Cooper, R. Differential stress induced melt migration: an experimental approach, *J. Geophys. Res.*, 95, 69796992, 1990.

[6] Forsyth, D., D. S. Scheirer, S. C. Webb et al. Imaging the deep seismic structure beneath a mid-ocean ridge: the melt experiment, *Science*, *280*, 1215-1218, 1998.

[7] Guillot, B., Sator, N., A computer simulation study of natural silicate melts. Part II: High pressure properties *Geochem. et cosmochem acta*, *71*, 4538-4556, 2007.

[8] Hall, C.E., E.M. Parmentier, Spontaneous melt localization in a deforming solid with viscosity variations due to water weakening, *Geophys. Res. Lett.27*, 9-12, 2000.

[9] Hammond, W.C., D. R. Toomey, Seismic velocity anisotropy and heterogeneity beneath the Mantle Electromagnetic and Tomography Experiment (MELT) region of the East Pacific Rise from analysis of P and S body waves, *Jour. of Geophys. Res.*, *108*, doi:10.1029/2002JB001789, 2003.

[10] Hess, P.C., in Mantle Flow and Melt Generation at Mid Ocean Ridges, J. Phipps-Morgan, D. K. Blackman, J. Sinton, Eds. (American Geophysical Union, Washington, DC), 67-102, 1992.

[11] Hirth, G., and D. Kohlstedt, Rheology of the upper mantle and the mantle wedge: A view from the experimentalists, in Inside the Subduction Factory, edited by J. Eiler, 83105, AGU, Washington, D.C., 2003.

[12] Holtzman B.K., Kohlstedt D.L., Stress-driven melt segregation and strain partitioning in partially molten rocks: Effects of stress and strain, *Jour. of Petrol.*, *48*, 2379-2406, 2007.

[13] Holtzman, B., Groebner, N., Zimmerman, M., Ginsberg, S., Kohlstedt, D., Stress-driven melt segregation in partially molten rocks, *Geochem. Geophys. Geosyst.*, *4*, Art. No. 8607, 2003.

[14] Karato, S., Wu, P., Rheology of the upper mantle: A synthesis, *Science*, *260*, 771-778, 1993.

[15] Katz R.F., Spiegelman M., Holtzman B., The dynamics of melt and shear localization in partially molten aggregates, *Nature*, *442*, 676-679, 2006.

[16] Korenaga, J; Karato, S.I., A new analysis of experimental data on olivine rheology, *Jour. Geophys. Res.*, *113*, B02403, doi:10.1029/2007JB005100, 2008.

[17] McKenzie, D., The Generation and Compaction of Partially Molten Rocks, *Jour. Petrol.*, *25*, 713-765, 1984.

[18] Mei, S., Bai, W., Hiraga, T., Kohlstedt, D., Influence of melt on the creep behavior of olivine-basalt aggregates under hydrous conditions, *Earth Planet Sci. Lett.*, *201*, 491-507, 2002.

[19] Morgan, J.P., Melt migration beneath mid-ocean spreading centers, *Geophys. Res. Lett.*, *14*, 12381241, 1987.

[20] Renner, J., Visckupic, K., Hirth, G. Evans, B., Melt extraction from partially molten peridotites, *Geochem. Geophys. Geosyst.*, *4*, 8606, doi:10.1029/2002GC000369, 2003.

[21] Richardson, C. Melt flow in a variable viscosity matrix, *Geophys. Res. Lett.*, 25, 10991102, 1998.

[22] Scott, D.R, and Stevenson, D.J., Magma Solitons, *Geophys. Res. Lett.*, *11*, 1161-1164, 1984.

[23] Scott, D.R., Stevenson, D.J., Magma ascent by porous flow, *Jour. Geophys. Res.*, *91*, 9283-9296, 1986.

[24] Sparks, D.W. and Parmentier, E.M., Melt extraction from the mantle beneath spreading centers, *Earth Planet Sci. Lett.*, *105*, 368-377, 1991.

[25] Spiegelman, M., Linear analysis of melt band formation by simple shear, *Geochem. Geophys. Geosys.*, *4*, Article 8615, doi:10.1029/2002GC000499, 2003.

[26] Spiegelman, M., Flow in deformable porous media. Part 1 Simple analysis, *Jour. Fluid Mech.*, *247*, 17-38, 1993.

[27] Spiegelman, M., McKenzie, D., Simple 2-D models for melt extraction at mid-ocean ridges and island arcs, *Earth Planet. Sci. Lett.*, *83*, 137152, 1987.

[28] Stevenson, D., Spontaneous small-scale melt segregation in partial melts undergoing deformation, *Geophys. Res. Lett.*, *16*, 10671070, 1989.

[29] Vera, E.E., Mutter J.C., Buhl, P., et al., The Structure of 0-MY to 0.2-MY old oceanic-crust at 9-degrees-n on the east pacific rise from expanded spread profiles, *Jour. Geophys. Res.*, 95, 15529-15556, 1990.

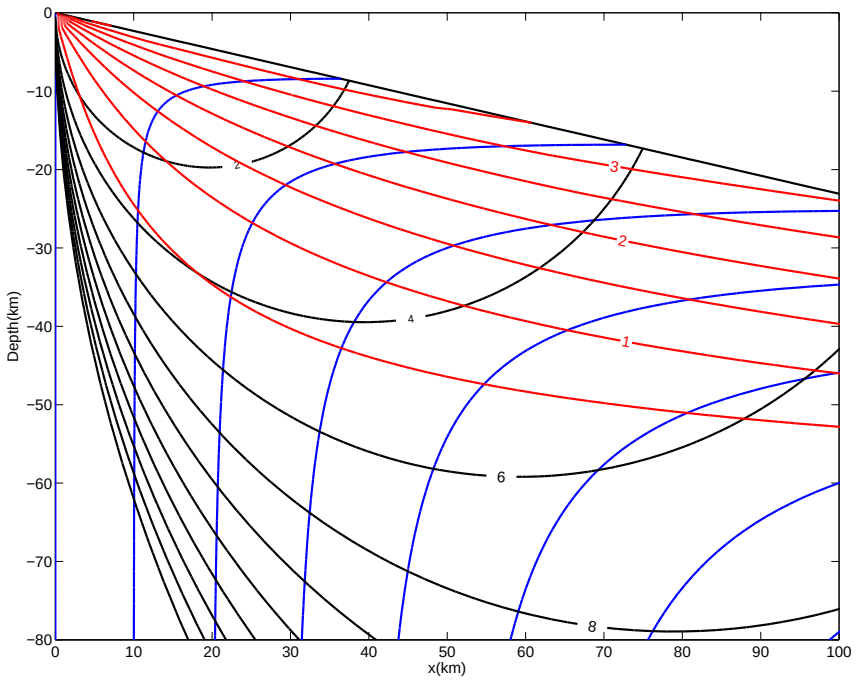

Fig. 1. Stream lines (blue), contours of constant B_u (black) and integrated strain (red) in the top 80 km near a fast spreading ridge.

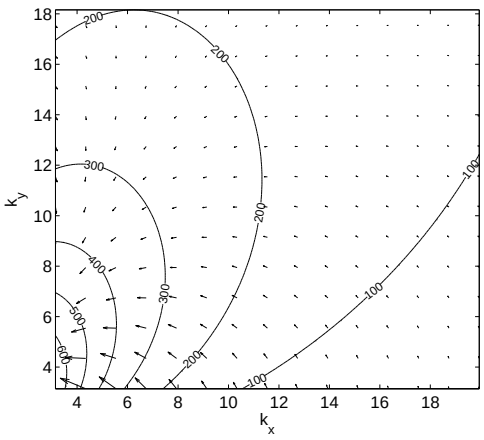

Fig. 2. Contours of the angular oscillation frequency, ω, with an overlain arrow plot of the group velocity for a calculation with $\phi_0 = 0.01$, $\zeta_0 = 1$ and $n_v = 6$.

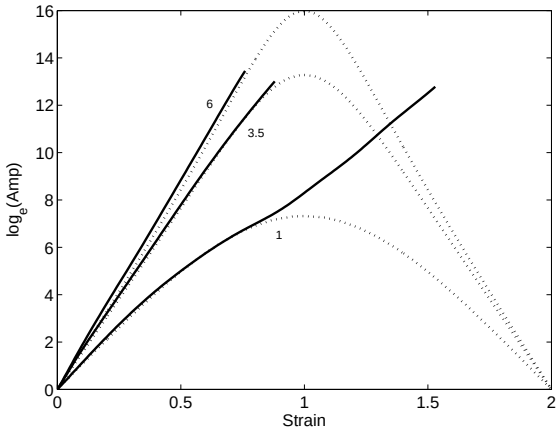

Fig. 3. Comparison of the amplitude of melt bands for the numerical model (solid) and linear theory (dotted) for $n_v = 1$, 3.5 and 6 with a single plane-wave initial condition.

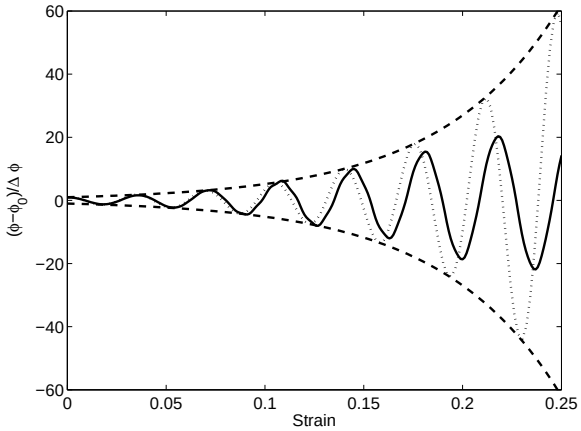

Fig. 4. Normalized porosity at a point calculated from the numerical model (solid line) and the prediction of linear theory (dotted line) as well as the linear prediction for the amplitude envelope (dashed line).

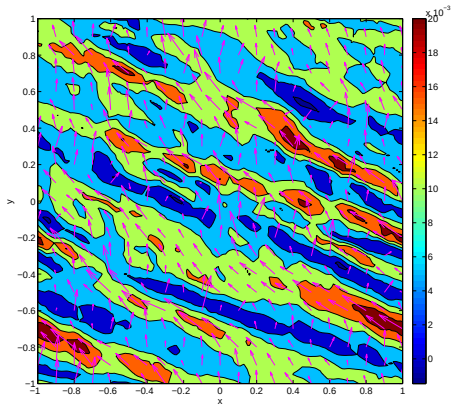

Fig. 5. Porosity field with an overlain arrow plot of the fluid velocity after a strain of 0.88 for a calculation with $n_v = 6$ and $B_u = 0.1$.

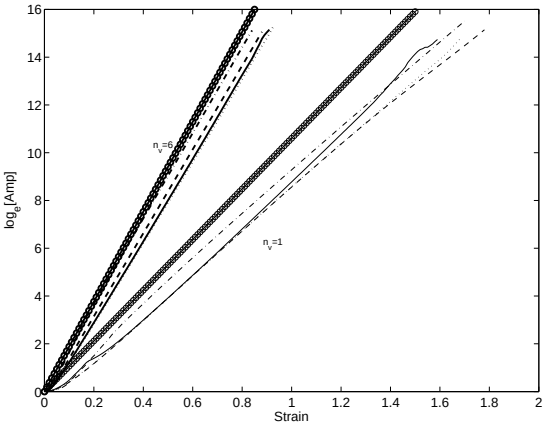

Fig. 6. The natural logarithm of the root-mean-square amplitude of the porosity variation as a function of time for simulations with $n_v = 1$ (thin lines) and $n_v = 6$ (thick lines). Buoyancy numbers are 0 (dash-dot line), 0.1 (dashed line), 1 (dotted line) and 10 (solid line). The circles indicate the amplitude of bands growing at the orientation of maximum growth rate for large $|k|$ predicted from equation 9.

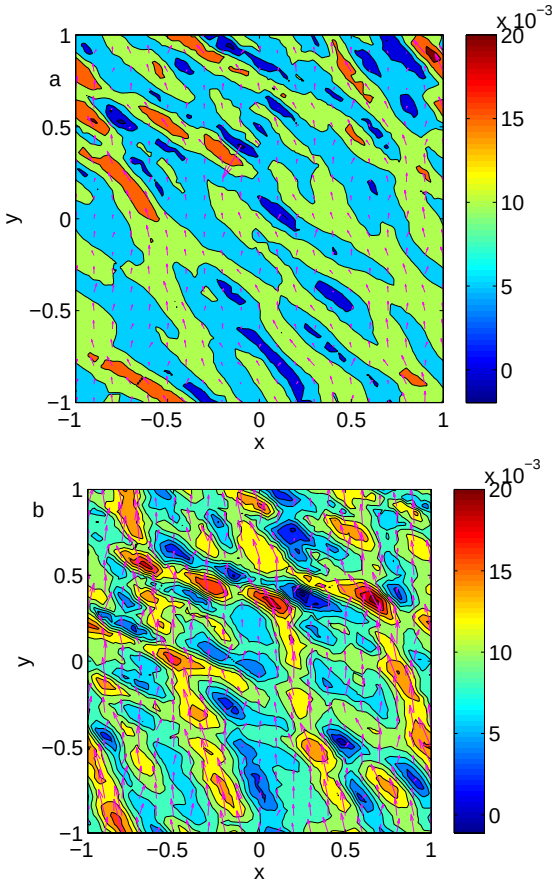

Fig. 7. Porosity field with an overlain arrow plot of the fluid velocity for calculations with $B_u = 10$. a) after a strain of 1.07 for a calculation with $n_v = 3.5$ and $B_u = 10$. and b) after a strain of 0.9 for a calculation with $n_v = 6$.

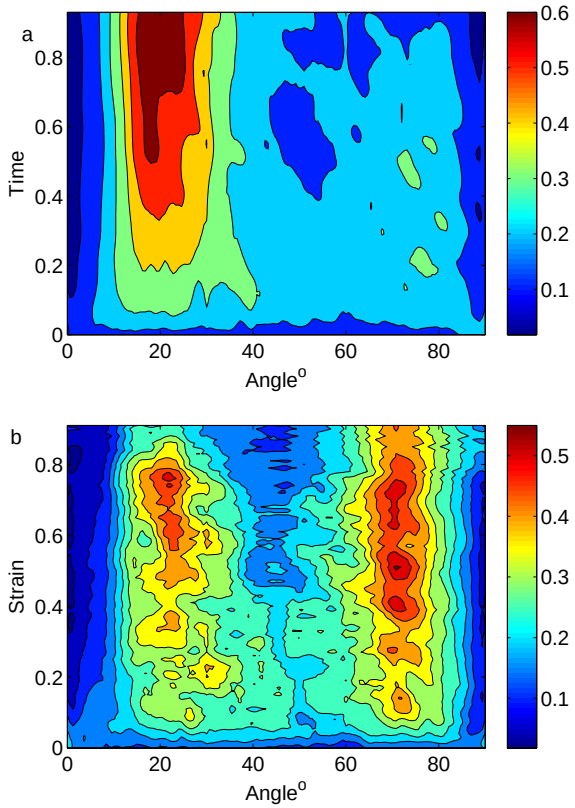

Fig. 8. Power spectra as a function of angle and as a function of time for calculations with $n_v = 6$ and a) $B_u = 0.1$ and b) $B_u = 10$.

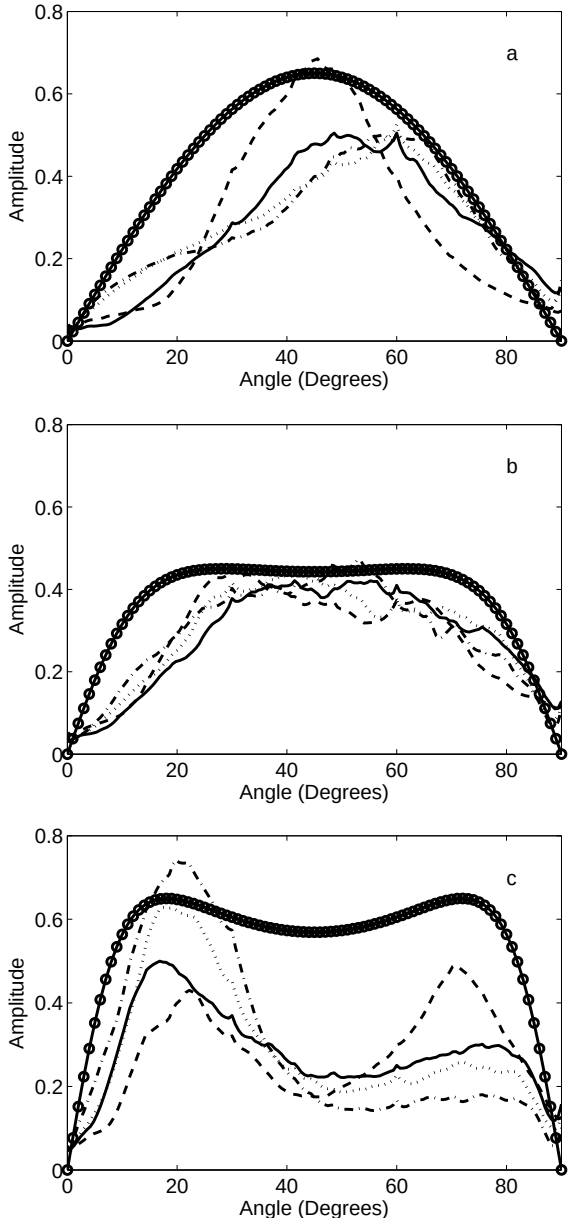

Fig. 9. Power spectrum as a function of angle averaged over the latter half of simulations with a) $n_v = 1$, b) $n_v = 3.5$ and c) $n_v = 6$ and $B_u = 0$ (dashed-dot line), 0.1 (dotted line), 1 (solid line) and 10 (dashed line). The solid line with circles is the instantaneous growth rate as a function of angle calculated from linear theory for large $|k|$.

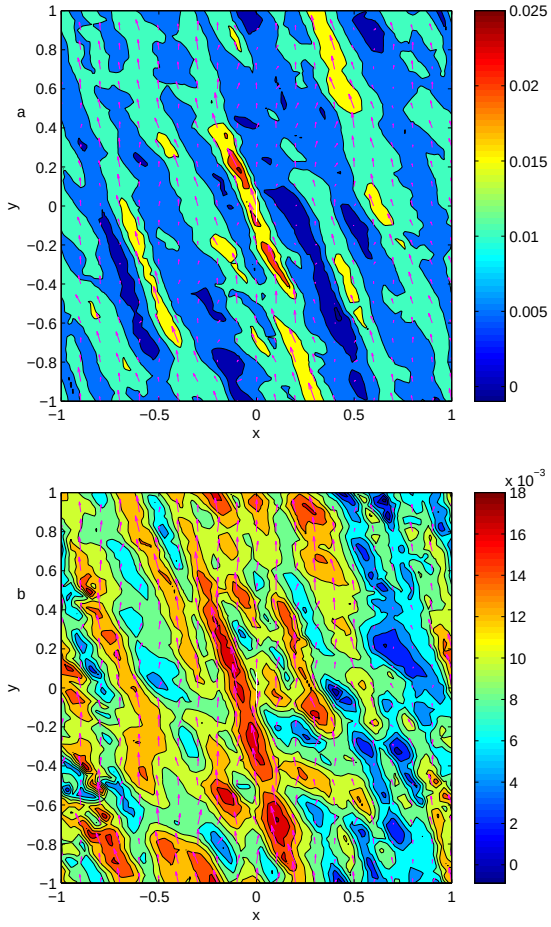

Fig. 10. Porosity field with an overlain arrow plot of the fluid velocity for calculations with $n_v = 6$ and with gravity parallel to the shear plane at a total strain of 0.92. In a) $B_u = 0.1$ and b) $B_u = 10$.

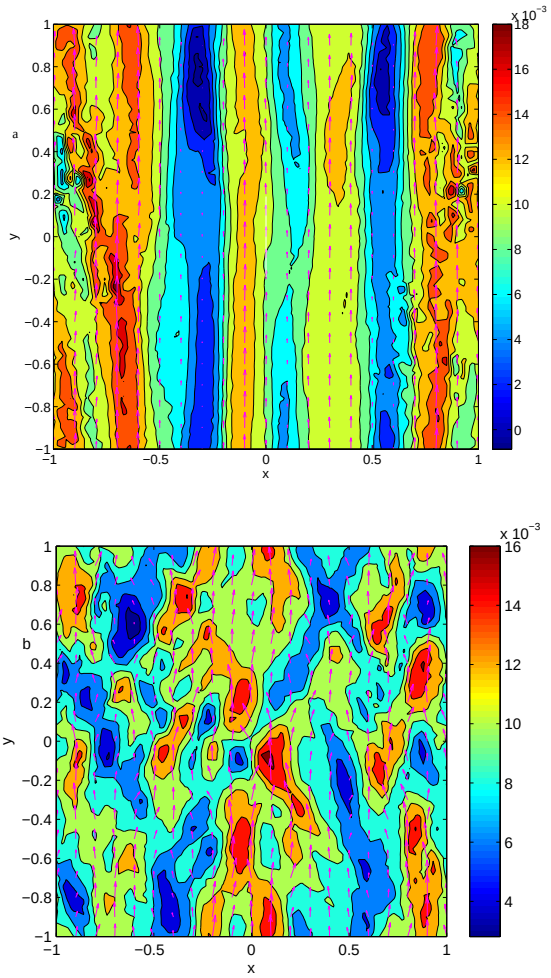

Fig. 11. Porosity field with an overlain arrow plot of the fluid velocity for calculations with a pure shear background velocity and $B_u = 10$. In a) $n_v = 1$ and the total strain is 0.8 and b) $n_v = 6$ and the total strain is 0.68.